

Single-field slice-imaging with a movable repeller: Photodissociation of N₂O from a hot nozzle

Dan J. Harding, J. Neugeboren, M. Grütter, A. F. Schmidt-May, D. J. Auerbach, T. N. Kitsopoulos, and A. M. Wodtke

Citation: *The Journal of Chemical Physics* **141**, 054201 (2014); doi: 10.1063/1.4891469

View online: <http://dx.doi.org/10.1063/1.4891469>

View Table of Contents: <http://scitation.aip.org/content/aip/journal/jcp/141/5?ver=pdfcov>

Published by the AIP Publishing

Articles you may be interested in

[Zero kinetic energy photoelectron spectroscopy of triphenylene](#)

J. Chem. Phys. **140**, 244308 (2014); 10.1063/1.4884905

[Laser initiated reactions in N₂O clusters studied by time-sliced ion velocity imaging technique](#)

J. Chem. Phys. **139**, 044307 (2013); 10.1063/1.4816008

[Conformer specific dissociation dynamics of iodocyclohexane studied by velocity map imaging](#)

J. Chem. Phys. **135**, 094312 (2011); 10.1063/1.3628682

[NO⁺ formation pathways in dissociation of N₂O⁺ ions at the C₂⁺ state revealed from threshold photoelectron-photoion coincidence velocity imaging](#)

J. Chem. Phys. **134**, 054312 (2011); 10.1063/1.3549130

[Single-photon and resonance-enhanced multiphoton threshold ionization of the allyl radical](#)

J. Chem. Phys. **131**, 014304 (2009); 10.1063/1.3157185



AIP | Journal of
Applied Physics

Journal of Applied Physics is pleased to
announce **André Anders** as its new Editor-in-Chief

Single-field slice-imaging with a movable repeller: Photodissociation of N₂O from a hot nozzle

Dan J. Harding,¹ J. Neugeboren,¹ M. Grütter,¹ A. F. Schmidt-May,¹ D. J. Auerbach,¹ T. N. Kitsopoulos,^{1,2,a)} and A. M. Wodtke^{1,a)}

¹*Institute for Physical Chemistry, Georg-August University of Göttingen, 37077 Göttingen, Germany and Max Planck Institute for Biophysical Chemistry, Göttingen, Germany*

²*Department of Chemistry, University of Crete, 71003 Heraklion, Greece and Institute of Electronic Structure and Laser, Foundation for Research and technology-Hellas, 71003 Heraklion, Greece*

(Received 13 May 2014; accepted 16 July 2014; published online 4 August 2014)

We present a new photo-fragment imaging spectrometer, which employs a movable repeller in a single field imaging geometry. This innovation offers two principal advantages. First, the optimal fields for velocity mapping can easily be achieved even using a large molecular beam diameter (5 mm); the velocity resolution (better than 1%) is sufficient to easily resolve photo-electron recoil in (2 + 1) resonant enhanced multiphoton ionization of N₂ photoproducts from N₂O or from molecular beam cooled N₂. Second, rapid changes between spatial imaging, velocity mapping, and slice imaging are straightforward. We demonstrate this technique's utility in a re-investigation of the photodissociation of N₂O. Using a hot nozzle, we observe slice images that strongly depend on nozzle temperature. Our data indicate that in our hot nozzle expansion, only pure bending vibrations – (0, ν_2 , 0) – are populated, as vibrational excitation in pure stretching or bend-stretch combination modes are quenched via collisional near-resonant V-V energy transfer to the nearly degenerate bending states. We derive vibrationally state resolved absolute absorption cross-sections for (0, $\nu_2 \leq 7$, 0). These results agree well with previous work at lower values of ν_2 , both experimental and theoretical. The dissociation energy of N₂O with respect to the O(¹D) + N₂¹ Σ_g^+ asymptote was determined to be 3.65 ± 0.02 eV. © 2014 AIP Publishing LLC. [<http://dx.doi.org/10.1063/1.4891469>]

I. INTRODUCTION

Since its introduction, ion imaging¹ and its later variants velocity mapping² and slice imaging,^{3–5} have been implemented by a large number of research laboratories around the world, spanning a diverse range of research fields.^{6,7} In this paper we present our recently constructed imaging apparatus at the Institute for Physical Chemistry at the University of Göttingen. By using the combination of a rimmed movable repeller electrode and a flat ultrafine mesh extractor, this molecular beam machine is capable of simple and rapid switching between ion-imaging (spatial imaging) and velocity map imaging (VMI) or slice imaging (SI). Our first application described in this paper involves the study of the ultraviolet photodissociation of N₂O at ~ 203.5 nm.

N₂O is an important atmospheric gas, which plays a major role in both ozone depletion and global warming.^{8–10} N₂O is linear in its ground state and therefore has three fundamental frequencies, a low-frequency doubly-degenerate bend, ν_2 , at 588.8 cm^{-1} , a symmetric N-O stretch, ν_1 , at 1285.0 cm^{-1} and an asymmetric N-N stretch, ν_3 , at 2223.5 cm^{-1} .¹¹ Its lowest electronic absorption band has an onset around $45\,000\text{ cm}^{-1}$ ($\sim 220\text{ nm}$), and peaks around $55\,000\text{ cm}^{-1}$ (180 nm).¹² The molecule is bent ($\sim 110^\circ$) in its first excited electronic state. While photon absorption by

the linear ground-state to form this excited electronic state is formally forbidden within the C_{∞v} point group, the transition becomes increasingly allowed as the molecule bends. Hence photo-absorption is strongly enhanced for vibrationally excited levels with bending excitation. Also due to the large change in NNO angle upon photoexcitation, N₂ photoproducts are formed with a large amount of rotational excitation ($60 < J < 80$). In recent years N₂O has been subject to a number of high resolution experiments^{13–16} using VMI,^{17–22} as well as high level theoretical calculations.^{23–32}

In the most recent VMI study of Suzuki and co-workers,²² the authors ionized individual rotational states of the N₂ photoproduct. Velocity map images showed three distinct velocities, corresponding to photodissociation of the three lowest vibrational states (0, $\nu_2 \leq 2$, 0) of N₂O, which were populated in the molecular beam expansion. Using an effusive beam where the vibrational temperature could be fixed at room temperature (300 K), the relative absorption cross sections for the (0, 1, 0) and (0, 2, 0) states with respect to the (0, 0, 0) state were derived. First principles calculations of *absolute* cross sections for individual vibrational levels (ν_1 , ν_2 , ν_3) by Schinke and co-workers reproduce these experimental findings and predict vibrationally resolved photo-absorption cross-sections for higher vibrational states.^{29–31}

In this work, we photodissociate vibrationally excited N₂O produced from a hot-nozzle, supersonic expansion. The high vibrational temperature ($T_{\text{vib}} = 700\text{ K}$) produced in this expansion in combination with the velocity resolution of the

^{a)}Authors to whom correspondence should be addressed. Electronic addresses: tkitsop@mpibpc.mpg.de and alec.wodtke@mpibpc.mpg.de

new VMI apparatus allows us to derive the relative vibrational state specific photoabsorption cross-sections for N_2O up to $(0, \nu_2 \leq 7, 0)$. Our derived absorption cross-sections agree with previous theoretical and experimental work where comparisons can be made and extend our knowledge of the photoabsorption of vibrationally excited N_2O to higher energy.

II. EXPERIMENTAL

The apparatus is shown in Fig. 1. It consists of three regions: the source, the differential pumping chamber, and the detector region. Briefly, a miniaturized source chamber is pumped using a 300 l/s maglev turbo-molecular pump. It is differentially pumped through a skimmer (Beam Dynamics Model 2) with a 2 mm orifice – the differential pumping region is also pumped using a 300 l/s maglev turbo-molecular pump. The differential pumping and detector chambers are separated by a 3 mm orifice. The detector chamber is pumped using a 1000 l/s maglev turbo-molecular pump. A molecular beam of the gas of interest is produced using a General Valve (Parker Series 9) with a 1 mm orifice, operating at 10 Hz and stagnation pressures from 1 to 3 bar are used. Typical operating pressures in the source chamber are 5×10^{-5} mbar.

The detector region hosts the ion optics used to perform ion imaging¹ velocity mapping² or slice imaging³. The ion optics are a modified version of the single field extraction design described by Papadakis *et al.*,³³ in which a rim on the repeller and extractor electrodes was used to create the appropriate curvature of the electric field contour lines in the ion acceleration region, such that VMI conditions are achieved at a specific point in space. In the work presented here, we have added some extra features to this design as shown in Fig. 2.

The main new features are: (a) the separation distance between the repeller and extraction electrode can be varied in vacuum, (b) the extractor electrode³⁴ is electrically isolated, i.e., it can be floated to a desired voltage, and (c) an additional three element (slit) einzel lens is placed after the acceleration region. This einzel lens was present in the original SI paper by Gebhardt *et al.*,³ before single field VMI/SI was introduced.³³ We explain the reason for reintroducing this feature below. The electrical “floating” option on the extractor electrode allows Wiley McLaren³⁵ time of flight focusing conditions to

be realized in situations where high mass resolution is desired or when very large unfocused laser beams are used for photodissociation or photoionization of the product.

A. Movable repeller electrode

The overall dimensions of the electrodes are specified in Fig. 2. The diameter is large (130 mm), in order to have the grounded support rods far away from the interaction region to reduce field distortions.³⁶ Movement of the repeller electrode is accomplished by a “lab-jack” screw-type arrangement as shown in Fig. 2. The threaded rod is $\text{M6} \times 1.0$, with left- and right-handed threads on opposing ends. Motion to this rod is provided manually under vacuum via a 6 mm rod coupled to the vacuum through a standard 6 mm cajon fitting. A universal joint is used to allow for the mismatch in alignment between the rod position and the position of the Cajon feedthrough. The VMI condition depends on the position of the ionization volume, i.e., the spatial alignment of the laser, between the repeller and extractor electrodes, as described by Papadakis *et al.*³³ The advantage of the movable electrode introduced here is that slight misalignment of the laser positions can be compensated for by adjusting the repeller position. Although, in principle, moving the laser beam/focus to the appropriate position is possible, in practice, when multiple laser beams are involved, repositioning and re-overlapping the laser beams can be cumbersome.

Spatial imaging conditions can be realized by making the separation between the repeller and extractor plates large enough such that the electrostatic contours become flat in the region where ions are generated. In our machine, the contours remain flat for repeller displacements from the extractor of 1 cm or more. In practice, the condition for spatial imaging is realized when the “appearance/size” of the image of a parent molecule (no recoil velocity) stops changing with further increase of the repeller-extractor separation. For example, when imaging the parent molecular beam (a reminder here that the molecular beam is pointed at the imaging detector and the extraction of the ions is also parallel to this direction, defined as Z) in VMI mode the parent beam image is a round spot 3–5 pixels in diameter. When we move away from VMI conditions, by increasing the repeller-extractor separation, the image becomes more cigar-shaped, namely longer in the direction of laser propagation (Y-direction). This is

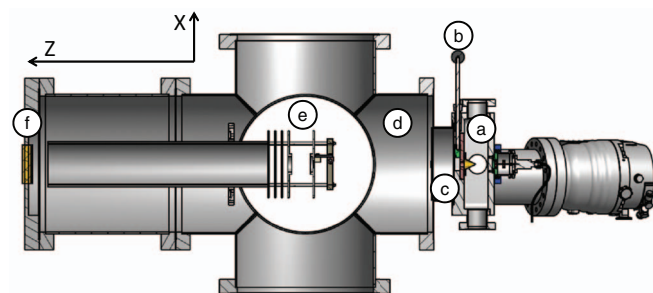


FIG. 1. A schematic of the newly constructed experimental apparatus. (a) Source region, (b) slide valve for isolating the source chamber, (c) differential pumping region, (d) detector region, (e) ion optics stack, and (f) imaging detector.

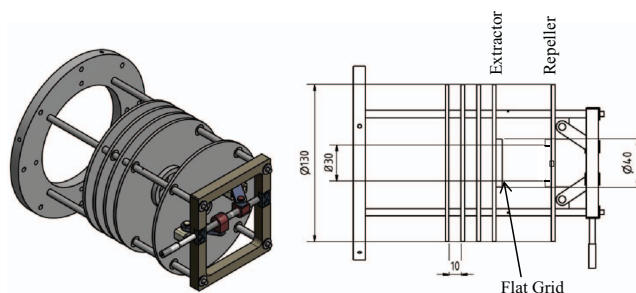


FIG. 2. Ion optics that include movable repeller electrode. Conditions for spatial imaging or VMI are achieved by adjusting the position of this electrode. The three element Einzel lens can be used for further VMI adjustment. Units are in mm.

because our ionization volume is determined by the shape of the laser beam near its focus. A confocal parameter of between 5 and 10 mm means that ions are produced over the entire width (5 mm in our case) of the molecular beam in the Y-direction, while in the X-direction, the dimension of the laser focus is typically sub-mm, hence the cigar shape. Once the size of this image becomes invariant to any further change in the repeller position, this signifies that spatial imaging mode has been achieved.

B. Einzel lens

Slice Imaging (SI) is achieved by using a delayed acceleration of the ions with respect to the ionization.³ We have reintroduced the Einzel lens after the acceleration region in order to have the ability for additional fine adjustment to the VMI condition. In situations where the velocity of the molecular beam is high enough so that the overall center of mass position of the system has moved sufficiently far away (≥ 1 mm) from the original VMI position, the VMI conditions can be re-established either by changing the repeller position or by applying a small voltage to the Einzel lens.

C. Imaging system

The detector is a Photonis 75 mm effective diameter imaging detector, with a fiber optic coupled phosphor screen (P47) and has been used in earlier VMI studies.^{37–39} Time-of-flight spectra can be recorded by AC coupling the output of the back channel plate just before the phosphor screen. In continuous operation (no pulsing of the detector) the front MCP is held at ground and the back MCP is held at about +1500 V, while a +6 kV potential is applied to the phosphor screen. These conditions are sufficiently sensitive to detect single ion events. When imaging of a specific mass is desired, in order to record a slice image, a narrow pulse of –850 V is applied to the front MCP using a home built HV-switch⁶ while the back MCP is held at +1000 V. It is stressed here that the large area of the channel plates increases the effective capacitance of the system, and longer pulses are necessary in order to have the front MCP reach the necessary voltage for effective single ion detection. Specifically, we note that a minimum of a 40–50 ns pulse-width is required for our 75 mm detector, but that we observe effective time slices of about 10 ns, as confirmed by the change in the appearance of the image as a function of time delay.

The camera and image acquisition software are LaVision, Imager E-lite 1600 × 1200 pixel CCD Camera and DaVis v.8. The software allows for event counting⁴⁰ in real time during the acquisition and the resolution enhancement this provides is discussed later in this paper.

D. Laser system

The laser system used in this study consists of a Nd:YAG (Spectra Physics Pro 250) operating at 10 Hz, 532 nm, pumping a dye laser system (Sirah Precision Scan) equipped with a

tripling unit, producing laser light with wavelengths between 200 and 215 nm with output power of 1–10 mJ.

E. Hot nozzle

A SiC tube, 30 mm long, with 2.2 mm outer, and 1 mm inner diameter is mounted on the exit of the General Valve.^{14,41} Current flows through the last 15 mm of the tube, typically 0.5–1 A, and makes this section of the tube glow orange-red. Although this arrangement is based on the Chen pyrolysis source, used primarily for the generation of various free radicals,⁴¹ our aim is to have efficient vibrational heating of the parent molecules, thereby helping us to develop detection schemes for vibrationally excited molecules.

F. Magnetic shielding

The magnetic shielding of the free flight region necessary for photoelectron imaging is accomplished by a double layer of μ -metal comprised of two concentric cylinders of 0.5 mm wall thickness with diameters of 90 and 80 mm, between the ion optic stack and the imaging detector. Helmholtz coils are used to cancel the residual magnetic fields in the region of the ion optic stack.

III. RESULTS

A. N₂ product state distribution

In these experiments, the same laser pulse is used to photolyze the parent N₂O molecule and subsequently to detect the photofragment of interest using resonance-enhanced multiphoton ionization (REMPI). The N₂ products are detected using (2 + 1) REMPI using the $a''^1\Sigma_g^+ \leftarrow X^1\Sigma_g^+$ transition first reported by Lykke and Kay.^{42,43} The product state distributions of N₂ using a room temperature (RT) and a heated (hot) nozzle are shown in Fig. 3. The spectrum appears to be relatively insensitive to the nozzle temperature for $J < 70$ but for $85 > J > 70$ a clear nozzle temperature dependence is seen.

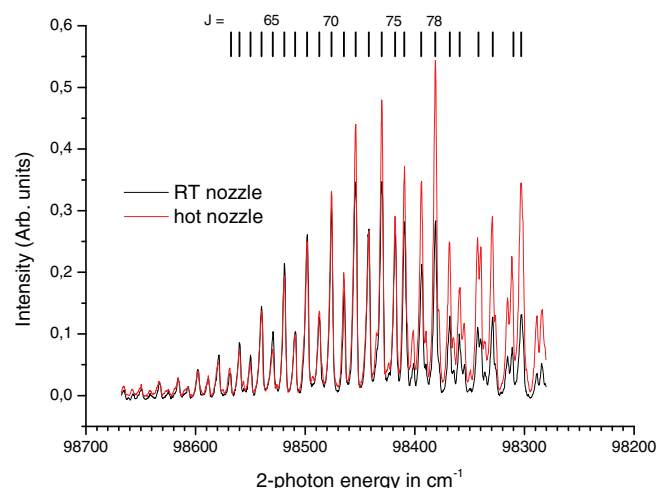


FIG. 3. (2 + 1) REMPI spectrum of N₂ formed by photodissociation of N₂O recorded using a room temperature nozzle (black) and heated nozzle (red). Tick marks indicate the corresponding rotational levels for N₂($v = 0, J$).

The most intense peak in the distribution shifts from $J = 74$ for the RT nozzle to $J = 78$ for the hot nozzle. An intensity alteration due to the nuclear spin statistics of N_2 between the odd- and even- J levels is observed. Most of the peaks are assigned to $N_2(v = 0)$ though several features in the spectrum appear irregular both in spacing and intensity.

B. $N_2(v, J)$ images

Slice velocity map images for the $N_2(v = 0, J = 78)$ product are shown in Fig. 4. We present only a quarter of the image, in order to facilitate the comparison between the RT and the hot nozzle images. Images are recorded with the laser polarization both parallel (z -direction) and perpendicular (x -direction) to the time-of-flight axis indicated in Fig. 1. Extraction delays of 400 ns are used to record these images. In the RT nozzle experiments, the image is dominated by a single ring; however, increasing the image contrast for visualization purposes makes it evident that rings at large radii are also present. In the hot nozzle, we notice that more rings appear at larger radii. Figures 4(c) and 4(d) show the kinetic

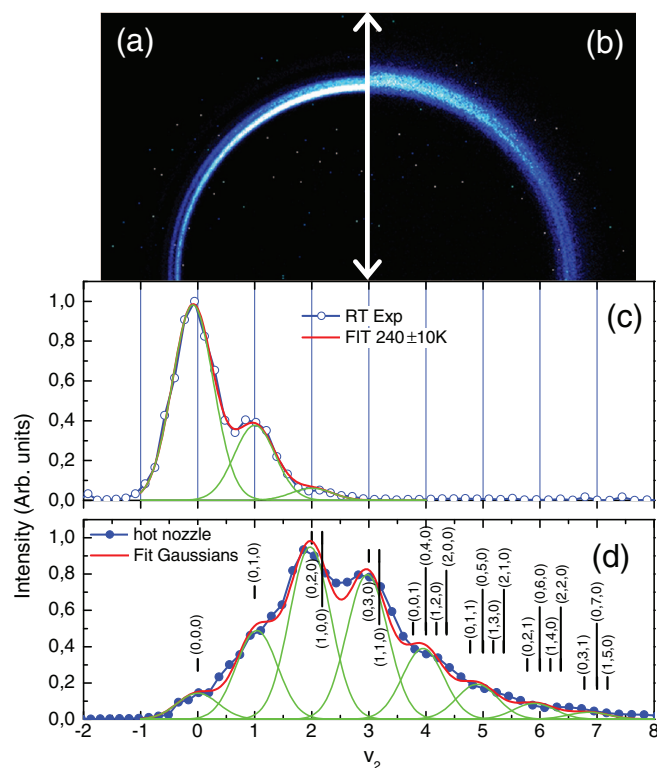


FIG. 4. Quadrants of the slice images for the photo-fragment $N_2(v = 0, J = 78)$ obtained using the room temperature (RT) and heated (hot) nozzle are shown in (a) and (b), respectively. The arrow indicates the direction of the laser polarization. The corresponding kinetic energy release spectra (KER) from these slice images are shown in (c) RT nozzle and (d) hot nozzle. The KER spectra have been calibrated and are shown in units of 589 cm^{-1} , the number of N_2O bending quanta. Tick marks indicate the positions for all possible vibrational states of N_2O in this energy range (v_1, v_2, v_3). The fit in (c) uses three Gaussian functions of common width, the theoretical cross sections from Ref. 29 for $v_2 = 0, 1, 2$ and Eq. (3) to determine the vibrational temperature of the sample. The fit in (d) uses seven Gaussian functions, centered at the energies of the pure bend excited states ($0, v_2, 0$) and using the width determined from (c). See text for details.

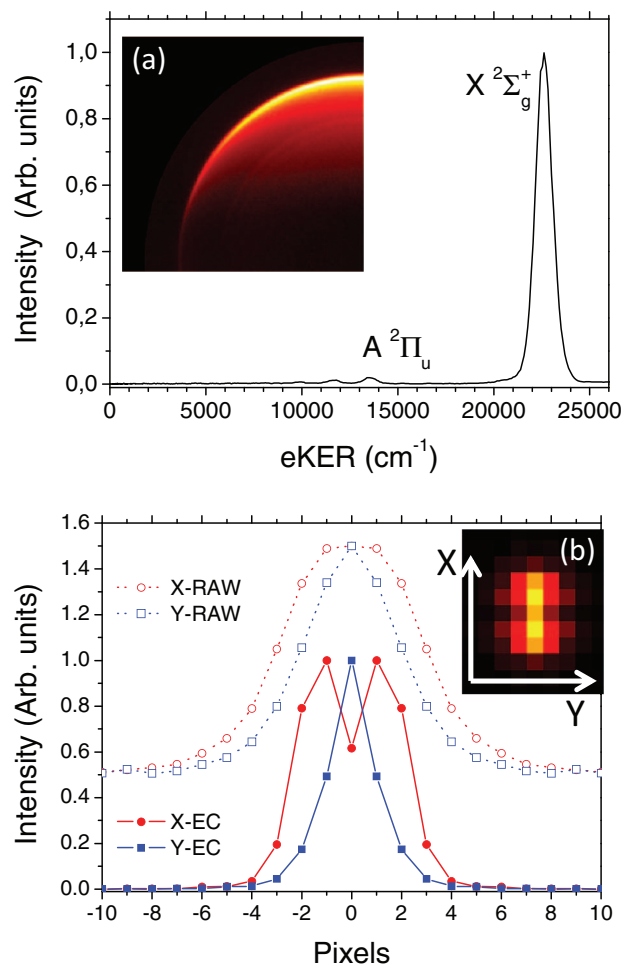


FIG. 5. (a) Photoelectron VMI of a molecular beam of cold $N_2(v = 0, J \sim 0)$ using $(2 + 1)$ REMPI at 203.2 nm and the corresponding photoelectron KER. The laser polarization is vertical (x direction). The term symbols correspond to the electronic states of the N_2^+ cation formed. (b) VMI using event counting (EC) of the N_2^+ formed in the photoionization process and intensity profiles of the images along the X (blue) vertical/laser polarization direction and Y (red) horizontal/laser propagation direction with and without (RAW) event counting.

energy release (KER) distributions derived from the data of Figs. 4(a) and 4(b) and is discussed later in the paper.

By careful observation of the rings in these images, we notice that the thickness of each ring is not uniform: We observe that it is thinner along the equator and thicker at the poles. This is a signature of photoelectron recoil.³⁶ To examine this more closely, the photoionization of a beam of pure N_2 was investigated. Photoelectron and photoion images were recorded and are shown in Figs. 5(a) and 5(b), respectively. The photoelectron energy spectrum is dominated by an ionization process that releases 2.8 eV in electron translational energy. In the N_2^+ image, Fig. 5(b), we clearly observe two resolved features.²² Their separation is 40 m/s consistent with recoil from a photoelectron with 2.8 eV of kinetic energy. We point out here that photoelectron recoil is only resolved when event counting (EC) is used. Taking intensity profiles from images with (EC) and without (RAW) event counting, we can fit a pair of Gaussian functions, whose half widths are ~ 3 and ~ 6 pixels for the EC and RAW images, respectively. The gain

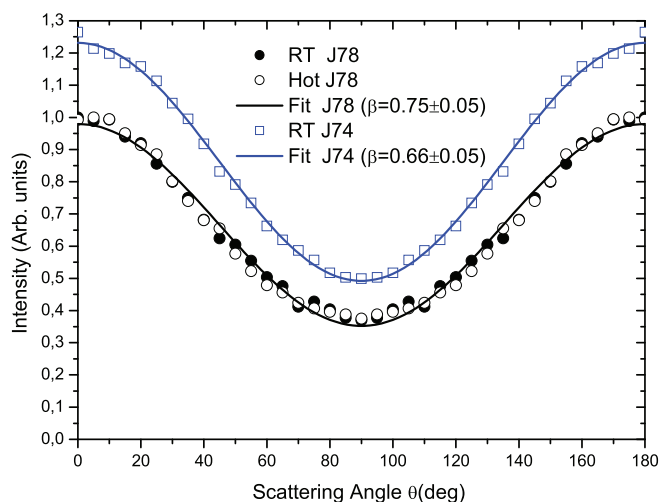


FIG. 6. Angular distributions for $N_2(v=0, J=74, 78)$ using a RT nozzle and angular distributions for $N_2(v=0, J=78)$ using a hot nozzle. The data are fitted using the relationship $I(\theta) \sim 1 + \frac{\beta}{2}(3 \cos^2 \theta - 1)$ and the corresponding β values are listed.

in velocity resolution is about a factor of 2 when EC is used. Photoelectron recoil is evident in intensity profiles through the slice images of $N_2(v=0, J=78)$, and with this we estimate that a velocity resolution of 1% is possible with our apparatus, limited by the photoelectron recoil, while the true velocity resolution of the instrument is less than 1%. We emphasize that this excellent velocity resolution is obtained for a large – 5 mm molecular beam diameter – ionization volume.

Angular distributions for $N_2(v=0, J=74, 78)$ photofragment states are shown in Fig. 6. The frequency of the probe laser was not scanned over the Doppler profile of the two-photon resonant excitation. In the case of $N_2(v=0, J=74)$ the angular distribution has been normalized using Z-images (laser polarization perpendicular to the imaging plane) in order to correct for any detector inhomogeneities and for the Doppler effect, while no such correction has been made to the distributions for $N_2(v=0, J=78)$ using RT and hot nozzles. The error introduced by not scanning over the Doppler profile is well within the uncertainty in the β value determination when fitting the data to the well-known relationship $I(\theta) \propto 1 + \frac{\beta}{2}(3 \cos^2 \theta - 1)$.⁴⁴

C. $O(^1D)$ images

KER spectra for the $O(^1D)$ photofragment are shown in Fig. 7, for both the RT and hot nozzle. These images are recorded by scanning over the Doppler profile of the REMPI excitation transition via the auto-ionizing 1P state. KER distributions are shown in Fig. 7. The RT nozzle spectra show partially resolved features when observed along the direction of the image where photoelectron recoil broadening is minimized $\theta \sim 90^\circ$, while in the case of experiments using a hot nozzle, these features can no longer be resolved and the overall distribution is shifted towards higher KER. As observed previously,^{14–22} when detecting $O(^1D)$ from the photolysis of N_2O via the auto-ionizing 1P state, for certain values of KER the intensity of the image peaks at angles other than 0° or 90° .

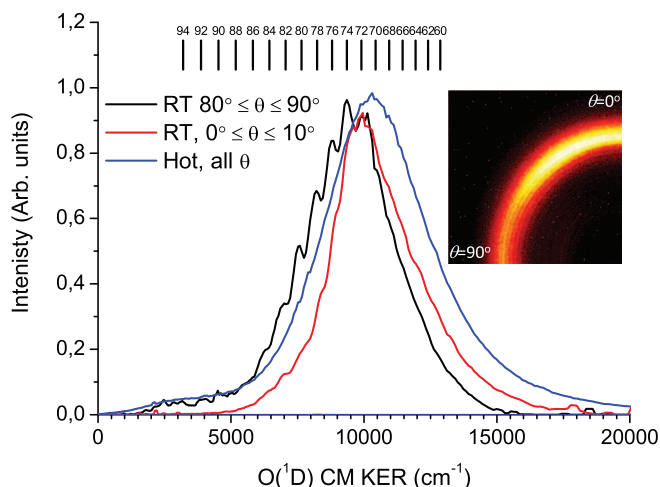


FIG. 7. KER spectra for the $O(^1D)$ photofragments obtained from the RT and hot nozzle. The insert shows a quadrant of the slice image obtained using the RT nozzle.

Since the corresponding sibling $N_2(J)$ photofragments do not show this effect, e.g., in Fig. 6 the angular distribution is maximum at $\theta = 0^\circ$, this has been attributed to a preferential alignment of the $O(^1D_2)$ atomic orbital with respect to the recoil velocity.¹⁹

IV. ANALYSIS AND DISCUSSION

Features in the KER spectra that are derived from images of single $N_2(v=0, J)$ product states produced in photodissociation of a cold beam of N_2O (Fig. 4(c)) have been assigned by Suzuki and co-workers²² to hot-bands; photodissociation from N_2O parent molecules in excited bending states leads to a larger N_2 kinetic energy. At first glance this might seem surprising – in light of the cooling often associated with supersonic expansion the population of vibrationally excited N_2O is small. However, the photo-physics of N_2O makes it extremely sensitive to bending excitations in the parent N_2O molecule. N_2O is linear in its ground electronic state ($X^1\Sigma^+$) and transitions to the low lying bent electronic states, the $2^1A'$ ($^1\Delta$) and $1^1A''$ ($^1\Sigma^-$), are forbidden in the linear geometry – term symbols at linearity are shown in the parentheses. Schinke and co-workers have extensively studied the photoexcitation of the molecule in this region and indicate that the absorption cross section increases dramatically as the amount of bending excitation increases.^{27–32} This explains why for a beam of cooled N_2O , even a small population in bending excited states can be seen by photodissociation. Experimental relative absorption cross sections $\sigma(v_2)$ for $v_2 = 0, 1, 2$ have been reported by Suzuki and co-workers²², while Schinke^{29,32} and co-workers have calculated absolute values for $\sigma(v_2)$ up to $v_2 = 4$.

The center of mass kinetic energy release during the photodissociation is given by the relationship,

$$KER_{N_2}(v=0, J=78) = (E_{ph} - D_0) + E_{N_2O}(v_2), \quad (1)$$

where E_{ph} is the photon energy, D_0 is the dissociation energy, and $E_{N_2O}(v_2)$ is the internal energy for N_2O assuming only

bending excitation, which is a good approximation for the RT nozzle. The size of the image in *pixels* is proportional to the photofragment speed so we can rewrite the equation in the form,

$$E_{N_2O}(v_2) - E_{ph} = -D_0 + B(\text{pixels})^2, \quad (2)$$

where B is the calibration scaling factor for our images. Assigning the 3 peaks observed in the RT image of Fig. 4(a) to photodissociation out of N_2O bend excited states – $v_2 = 0, 1$, and 2, respectively – we use Eq. (2) to obtain B and D_0 and subsequently the KER spectrum shown in Fig. 4(c). We use the same calibration parameters as in the RT nozzle images for calibrating the hot nozzle images. We determine a dissociation energy with respect to the $O(^1D) + N_2(^1\Sigma_g^+)$ asymptote of 3.65 ± 0.02 eV, which within our experimental uncertainty, agrees with the 3.63 eV value reported by of Suzuki and co-workers²¹ and is even closer to the 3.64 eV value reported by Okabe.⁴⁵

The intensity of each peak in the KER distribution of Fig. 4(c) is given then by the following relationship:

$$I \propto \sigma(0, v_2 \leq 2, 0)(v_2 + 1)e^{-\frac{\Delta E}{kT}}, \quad (3)$$

where $\sigma(0, v_2 \leq 2, 0)$ is the theoretical absorption cross section and ΔE is the vibrational excitation energy for the (v_1, v_2, v_3) mode, respectively, and $(v_2 + 1)$ is the degeneracy factor for bending vibrations. For the KER distribution derived from RT nozzle experiments, the fit using Eq. (3) is shown in Fig. 4(c); it yields a vibrational temperature of 240 ± 10 K, a reasonable expectation for a sample that has undergone partial vibrational relaxation in the molecular beam expansion. The quality of the fit is excellent showing outstanding agreement with the theoretical absorption cross sections for $v_2 = 0, 1$, and 2. We point out here that our experiment can only yield relative cross sections and the absolute scale is obtained by scaling our results to the theoretical values.

For our hot nozzle experiments, the vibrational population prior to expansion is thermal, but during expansion, partial collisional cooling is expected.⁴⁶ For N_2O this is relatively simple, since near resonant V-V vibrational energy transfer between the stretch and bend levels is expected to be extremely efficient as they are in Fermi resonance with one another.⁴⁷ As is evident in Fig. 4(d), bend-stretch combinations are nearly degenerate to the pure-bends for N_2O , and shock tube experiments have shown that relaxations between $(1, 0, 0) \rightarrow (0, 2, 0)$ $(0, 0, 1) \rightarrow (0, 2, 0)$ are both rapid and dominating at high temperatures.^{48,49}

This provides a means of determining the vibrational population distribution after expansion from the hot nozzle. Specifically, we assume that any population in stretch and stretch-bend combination levels rapidly relaxes into the nearly degenerate pure bending levels and that subsequently the pure bend levels may further relax slightly. The intensity pattern of the Gaussian peaks of Fig. 4(d) is then given by the relationship,

$$I \propto \delta(0, v_2, 0) \left[\sum (v_2 + 1) e^{-\frac{\Delta E(v_1, v_2, v_3)}{kT}} \right], \quad (4)$$

where the sum is over the nearly degenerate levels. Returning to Fig. 4(d), we use the relative intensities of the three Gaus-

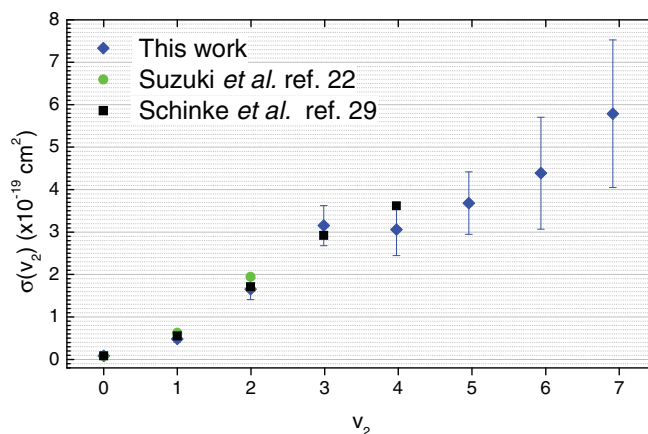


FIG. 8. Photoabsorption cross sections, $\sigma(0, v_2, 0)$, derived from this work, from theory (Schinke *et al.*²⁹) and from prior experiments (Suzuki *et al.*²²).

sians corresponding to $v_2 = 0, 1$, and 2, the known photoabsorption cross sections for these three states and Eq. (4) to obtain the vibrational temperature of the sample. This leads to a temperature of 700 ± 50 K for the hot KER spectrum. In an independent study we measured the vibrational temperature of acetylene from our hot nozzle by observing the REMPI detected population depletion from the ground state. This resulted in a similar vibrational temperature.

With this vibrational temperature in hand, the cross sections $\sigma(0, v_2 > 2, 0)$ were obtained using Eq. (4) and the individual Gaussian intensities. Our results are shown in Fig. 8, along with the theoretical results of Schinke and co-workers²⁹ and the experimental values for $\sigma(0, 0-2, 0)$ reported previously by Suzuki and co-workers.²² Both our results and those of Suzuki are relative measurements and the absolute scale shown in Fig. 8 is obtained from scaling to the absolute theoretical cross sections of Schinke. The agreement between theory (up to $v_2 = 4$) as well as previous experiments (up to $v_2 = 2$) is excellent. The observed initial strong increase in $\sigma(0, v_2, 0)$ is attributed to the increase in the transition dipole moment with the bending angle of the molecule.^{23,27,28} The incremental change in bond angle $\Delta\gamma$ is large for the first few vibrational bending levels as the molecule is linear in its ground vibrational state, but $\Delta\gamma$ is expected to become smaller (yet remain positive) as v_2 increases. This is qualitatively consistent with our measurements but extending the cross section calculations beyond $(0, 4, 0)$ to the higher vibrational levels probed by our experiment are necessary for direct comparison.

The structure appearing in the KER of $O(^1D)$ (Fig. 7) is assigned to rotational states of the $N_2(v = 0)$ co-fragment, following the work of Suzuki and co-workers.²² Only even J -states of N_2 are resolved, which are twice as populated as odd- J states. More interesting is the bi-modal nature of the KER distribution, consisting of a fast intense part between 5000 cm^{-1} and $20\,000 \text{ cm}^{-1}$ and a weaker contribution below 5000 cm^{-1} corresponding to $N_2(v = 0, J > 83)$. In Fig. 7 we observe that the relative intensity of the fast to slow components remains independent of nozzle temperature, while the change in the shape of the KER curve, including the 1300 cm^{-1} average shift towards higher KER, occurs only beyond

5000 cm^{-1} . Below 5000 cm^{-1} , the KER appears independent of nozzle temperature. A similar low energy tail in the KER was observed by Felder *et al.*¹³ in the photodissociation spectrum of N_2O at 193 nm. This raises the possibility that a second type of photodissociation dynamics is responsible for the low energy tail. The angular distributions for the slow region, i.e., $\text{N}_2(J > 83)$, changes dramatically from positive anisotropy parameters (β) for $\text{N}_2(J < 83)$ to nearly zero,^{18,19,22} providing further evidence that the photodissociation dynamics mechanism in this part of the KER spectrum could be different.

Angular distributions for both the $\text{O}(^1\text{D})$ and the $\text{N}_2(v = 0, J)$ levels have been discussed previously.^{18,19,22} We observe both atomic orbital alignment for the $\text{O}(^1\text{D})$ photofragment and a non-limiting β value for $\text{N}_2(v = 0, J)$, on average ~ 0.7 for J 's between 60 and 80, in agreement with previous results. Recent calculations predict that over 97% of the absorption at 204 nm involves excitation to the $2^1\text{A}'$ state, i.e., a parallel transition, which means the dipole moment lies in the plane of the molecule.^{23,25,26,28,31} This of course means the β values can vary dramatically depending on the direction of the transition dipole moment with respect to the N–O bond direction. Interpretations of the deviation of β from the limiting value invoked a non-axial recoil mechanism, especially as the KER becomes small.³¹ McBane *et al.*³¹ used surface hopping techniques to describe the non-adiabatic transitions between the excited $2^1\text{A}'$ state and the ground electronic state, which occur during the exit channel at relatively long $\text{N}_2\text{--O}$ bond distances. From classical trajectory calculations, they conclude that the reduction of β in the region $60 \leq J \leq 83$ is caused primarily from nonaxial recoil of the photofragments because of the significant torques on the excited state surface that cause the molecule to bend. During the surface hopping (non-crossing non-adiabatic transitions) from the bent excited state, back to ground electronic state, the molecule experiences additional forces, that cause further reduction of the anisotropy parameter. Comparison of the angular distributions for RT and hot nozzles, shown in Fig. 6, indicate no change in the β value, i.e., β does not depend on v_2 ,¹⁹ which means that angular distributions are essentially governed by the excited state dynamics. These results, i.e., both the $\beta(J)$ variation and the tail in the KER spectrum, seem to at least be in very good qualitative agreement with the conclusions of McBane *et al.*³¹

V. CONCLUSIONS

We have presented our new photofragment/photoelectron imaging spectrometer, which allows spatial imaging (original ion imaging), velocity mapping, and slice imaging of ions of photofragments, including H atoms. The resolution of the apparatus has been demonstrated to be better than 1% in velocity, even when large molecular beams are used such as 5 mm in diameter. We have used this apparatus to study the photofragmentation of N_2O at ~ 203.5 nm and we report on the relative absorption cross sections for bending excited state up to $v_2 = 7$. Our results are in excellent agreement with theoretical cross sections for individual vibrational quantum states up to $(0, 4, 0)$. This experiment demonstrates that photodisso-

ciation imaging experiments of molecules like N_2O constitute a sensitive probe of the vibrational state distribution of the parent molecules.

ACKNOWLEDGMENTS

This work is sponsored by Deutsche Forschungsgemeinschaft and the Alexander von Humboldt Professorship. A.M.W., T.N.K., and M.G. would like to acknowledge support from the Alexander von Humboldt Foundation. We thank Mr. Florian Lange for outstanding technical support. We also thank Professor Dr. R. Schinke for enlightening discussions concerning the photodissociation of N_2O and Dr. Bérenger Gans, Université Paris-Sud, for helpful discussions in the design and building of the Chen-pyrolysis source.

- ¹D. W. Chandler and P. L. Houston, *J. Chem. Phys.* **87**, 1445 (1987).
- ²A. T. J. B. Eppink and D. H. Parker, *Rev. Sci. Instrum.* **68**, 3477 (1997).
- ³C. R. Gebhardt, T. P. Rakitzis, P. C. Samartzis, V. Ladopoulos, and T. N. Kitsopoulos, *Rev. Sci. Instrum.* **72**, 3848 (2001).
- ⁴J. J. Lin, J. Zhou, W. Shiu, and K. Liu, *Rev. Sci. Instrum.* **74**, 2495 (2003).
- ⁵D. Townsend, M. P. Minitti, and A. G. Suits, *Rev. Sci. Instrum.* **74**, 2530 (2003).
- ⁶*Imaging in Molecular Dynamics*, edited by B. J. Whitaker (Cambridge University Press, Cambridge, 2003).
- ⁷M. N. R. Ashfold, N. H. Nahler, A. J. Orr-Ewing, O. P. J. Vieuxmaire, R. L. Toomes, T. N. Kitsopoulos, I. A. Garcia, D. A. Chestakov, S. M. Wu, and D. H. Parker, *Phys. Chem. Chem. Phys.* **8**, 26 (2006).
- ⁸R. P. Wayne, *Chemistry of Atmospheres*, 2nd ed. (Oxford University Press, Oxford, 1991).
- ⁹P. R. V. Forster, P. Artaxo, T. Bernsten, R. Betts, D. W. Fahey, J. Haywood, J. Lean, D. C. Lowe, G. Myhre, J. Nganga, R. Prinn, G. Raga, M. Schulz, R. Van Dorland, *Climate Change 2007: The Physical Science Basis*, edited by S. Solomon, D. Quin, M. Manning, Z. Chen, M. Marquis, K. B. Averyt, M. Tignor, H. L. Miller (Cambridge University Press, Cambridge, 2007), Contribution of Working Group I to the Fourth Assessment Report of the Intergovernmental Panel on Climate Change.
- ¹⁰A. R. Ravishankara, J. S. Daniel, R. W. Portmann, *Science* **326**, 123 (2009).
- ¹¹G. Herzberg, *Infrared and Raman Spectra* (Van Nostrand Reinhold, New York, 1945), p. 278.
- ¹²G. S. Selwyn and H. S. Johnston, *J. Chem. Phys.* **74**, 3791 (1981).
- ¹³P. Felder, B.-M. Haas, and J. R. Huber, *Chem. Phys. Lett.* **186**, 177 (1991).
- ¹⁴T. F. Hanisco and A. C. Kummel, *J. Phys. Chem.* **97**, 7242 (1993).
- ¹⁵L. L. Springsteen, S. Satyapal, Y. Matsumi, and P. L. Houston, *J. Phys. Chem.* **97**, 7239 (1993).
- ¹⁶T. Suzuki, H. Katayanagi, Y. X. Mo, and K. Tonokura, *Chem. Phys. Lett.* **256**, 90 (1996).
- ¹⁷M. Ahmed, E. R. Wouters, D. S. Peterka, O. S. Vasyutinskii, and A. G. Suits, *Faraday Discuss.* **113**, 425 (1999).
- ¹⁸D. W. Neyer, A. J. R. Heck, D. W. Chandler, J. M. Teule, and M. H. M. Janssen, *J. Phys. Chem. A* **103**, 10388 (1999).
- ¹⁹J. M. Teule, G. C. Groenenboom, D. W. Neyer, D. W. Chandler, and M. H. M. Janssen, *Chem. Phys. Lett.* **320**, 177 (2000).
- ²⁰A. G. Smolin, O. S. Vasyutinskii, E. R. Wouters, and A. G. Suits, *J. Chem. Phys.* **121**, 6759 (2004).
- ²¹T. Nishide and T. Suzuki, *J. Phys. Chem. A* **108**, 7863 (2004).
- ²²H. Kawamata, H. Kohguchi, T. Nishide, and T. Suzuki, *J. Chem. Phys.* **125**, 133312 (2006).
- ²³D. G. Hopper, *J. Chem. Phys.* **80**, 4290 (1984).
- ²⁴A. Brown, P. Jimeno, and G. G. Balint-Kurti, *J. Phys. Chem. A* **103**, 11089 (1999).
- ²⁵M. N. Daud, G. G. Balint-Kurti, and A. Brown, *J. Chem. Phys.* **122**, 054305 (2005).
- ²⁶S. Nanbu and M. S. Johnson, *J. Phys. Chem. A* **108**, 8905 (2004).
- ²⁷R. Schinke, J. Suarez, and S. C. Farantos, *J. Chem. Phys.* **133**, 091103 (2010).
- ²⁸R. Schinke, *J. Chem. Phys.* **134**, 064313 (2011).
- ²⁹J. A. Schmidt, M. S. Johnson, and R. Schinke, *Atmos. Chem. Phys.* **11**, 8965 (2011).
- ³⁰J. A. Schmidt, M. S. Johnson, U. Lorenz, G. C. McBane, and R. Schinke, *J. Chem. Phys.* **135**, 024311 (2011).

- ³¹G. C. McBane and R. Schinke, *J. Chem. Phys.* **136**, 044314 (2012).
- ³²R. Schinke, *Chem. Phys.* **399**, 142 (2013).
- ³³V. Papadakis and T. N. Kitsopoulos, *Rev. Sci. Instrum.* **77**, 083101 (2006).
- ³⁴The extractor electrode has a very flat grid 1000 lines-per-inch by Precision Electroforming, that is attached to the stainless steel “frame” using graphite conductive epoxy, Nr. 12691-30 Electron Microscopy Sciences.
- ³⁵W. C. Wiley and I. H. McLaren, *Rev. Sci. Instrum.* **26**, 1150 (1955).
- ³⁶R. L. Toomes, P. C. Samartzis, T. P. Rakitzis, and T. N. Kitsopoulos, *Chem. Phys.* **301**, 209 (2004).
- ³⁷N. Hansen and A. M. Wodtke, *Chem. Phys. Lett.* **356**, 340 (2002).
- ³⁸P. C. Samartzis, N. Hansen, and A. M. Wodtke, *Phys. Chem. Chem. Phys.* **8**, 2958 (2006).
- ³⁹Y. Y. Ji, S. P. K. Koehler, D. J. Auerbach, and A. M. Wodtke, *J. Vac. Sci. Technol., A* **28**, 807 (2010).
- ⁴⁰H. B. Y. Chang, R. C. Hoetzlein, J. A. Mueller, J. D. Geiser and P. L. Houston, *Rev. Sci. Instrum.* **69**, 1665 (1998).
- ⁴¹D. W. Kohn, H. Clauberg, P. Chen, *Rev. Sci. Instrum.* **63**, 4003 (1992).
- ⁴²K. R. Lykke, and B. D. Kay, *J. Chem. Phys.* **92**, 2614 (1990).
- ⁴³K. R. Lykke, and B. D. Kay, *J. Chem. Phys.* **95**, 2252 (1991).
- ⁴⁴R. N. Zare, *Mol. Photochem.* **4**, 1 (1972).
- ⁴⁵H. Okabe, *Photochemistry of Small Molecules* (Wiley, New York, 1978), p. 219.
- ⁴⁶G. Scoles, *Atomic and Molecular Beam Methods* (Oxford, Oxford, 1988), pp. 14–117.
- ⁴⁷J. D. Lambert, *Vibrational and Rotational Relaxation in Gases* (Calderon Press, Oxford, 1977).
- ⁴⁸Z. Baalbaki and H. Teitelbaum, *Chem. Phys.* **104**, 83 (1986).
- ⁴⁹R. T. V. Kung, *J. Chem. Phys.* **63**, 5305 (1975)